

**Shining Light on Dark Matter,  
One Photon at a Time**

by

Brandon Leigh Allen

Submitted to the Department of Physics  
in partial fulfillment of the requirements for the degree of

Doctorate of Science in Physics

at the

MASSACHUSETTS INSTITUTE OF TECHNOLOGY

June 2019

© Massachusetts Institute of Technology 2019. All rights reserved.

Author .....  
Department of Physics  
May 18, 2019

Certified by .....  
Christoph E.M. Paus  
Professor  
Thesis Supervisor

Accepted by .....  
Nergis Mavalvala  
Associate Department Head for Education



**Shining Light on Dark Matter,  
One Photon at a Time**

by

Brandon Leigh Allen

Submitted to the Department of Physics  
on May 18, 2019, in partial fulfillment of the  
requirements for the degree of  
Doctorate of Science in Physics

**Abstract**

A search is conducted for new physics in final states containing a photon and missing transverse momentum in proton-proton collisions at  $\sqrt{s} = 13$  TeV. The data collected by the CMS experiment at the CERN LHC correspond to an integrated luminosity of 35.9 inverse femtobarns. No deviations from the predictions of the standard model are observed. The results are interpreted in the context of dark matter production and limits on new physics parameters are calculated at 95% confidence level. For the two simplified dark matter production models considered, the observed (expected) lower limits on the mediator masses are both 950 (1150) GeV for 1 GeV dark matter mass.

Thesis Supervisor: Christoph E.M. Paus

Title: Professor



## Acknowledgments

This is the acknowledgements section. You should replace this with your own acknowledgements.



# Contents

<b>1</b>	<b>The Large Hadron Collider</b>	<b>9</b>
1.1	Experimental Apparatus . . . . .	9
1.2	Collider Phenomenology . . . . .	11
1.2.1	Parton Distribution Functions . . . . .	13
1.2.2	Hard Scattering . . . . .	14
1.2.3	Parton Shower . . . . .	14
1.2.4	Hadronization . . . . .	15
<b>2</b>	<b>The CMS Detector</b>	<b>17</b>
2.1	Inner Trackers . . . . .	19
2.2	Electromagnetic Calorimeter . . . . .	21
2.2.1	Preshower Detector . . . . .	23
2.3	Hadronic Calorimeter . . . . .	24
2.4	Muon Chambers . . . . .	26
2.5	Online Trigger System . . . . .	28
2.6	Detector Simulation . . . . .	29



# Chapter 1

## The Large Hadron Collider

### 1.1 Experimental Apparatus

The Large Hadron Collider (LHC) is a circular proton-proton collider, 27 km in circumference and between 40 and 175 m below the surface, located at the European Organization for Nuclear Research (CERN) on the French-Swiss border near the city of Geneva. Designed to collide protons at a maximum center-of-mass energy  $\sqrt{s} = 14 \text{ TeV}$ , the LHC has delivered collisions at  $\sqrt{s} = 7, 8 \text{ TeV}$  during Run 1 (2010-2012) and at  $\sqrt{s} = 13 \text{ TeV}$  during Run 2 (2015-2018). While the LHC is primarily a proton-proton collider, lead (Pb) ion beams of energy of up to 2.8 TeV per nucleon are used to produce lead-lead and proton-lead collisions. In this thesis, we focus exclusively on data recorded from proton-proton collisions during Run 2.

The LHC is the final stage of the CERN accelerator complex depicted in Figure 1-1. Hydrogen atoms are stripped of their electrons and accelerated to an energy of 50 GeV by the LINAC2 linear acceleration. Following this, they are injected into the Booster ring, the Proton Synchrotron (PS), and the Super Proton Synchrotron (SPS) and accelerated to 1.4, 26, and 450 GeV, respectively. After the SPS, the protons are injected into the two counter-circulating rings of the LHC in up to 2808 discrete bunches with a bunch spacing of 25 ns. The two beams intersect in eight places along the LHC with detector experiments CMS, ATLAS, LHCb, and ALICE each located at an intersection point.

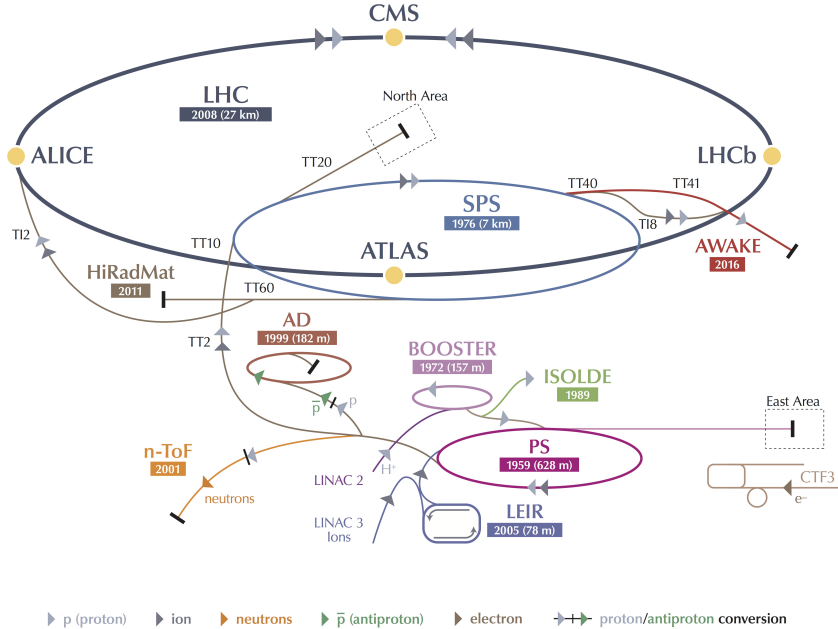


Figure 1-1: A schematic representation of the CERN accelerator complex. The LHC (dark blue) is fed protons by a chain of intermediate accelerators, beginning with LINAC2 (light pink). Reprinted from the CERN Document Server [1].

The LHC is a synchrotron containing 1232 superconducting NbTi dipole magnets measuring 15 m in length, each with a peak dipole field of 8.33 Tesla. There are an additional 492 quadrupole magnets measuring 5-7 m in length which focus the beams in between the dipole magnets. Due to space limitations in the tunnels, the beam pipes are magnetically coupled and the magnets share the same superfluid liquid helium cryostatic system to achieve the 1.9K temperature required to achieve the desired magnetic field strength.

The number of events produced at the LHC is given by

$$N(pp \rightarrow X) = \int dt L(t) \sigma(pp \rightarrow X), \quad (1.1)$$

where  $\sigma$  is the cross section of the process and  $L$  is the instantaneous luminosity of the machine given by

$$L = \frac{N_b^2 n_b f_{\text{rev}} \gamma}{4\pi \epsilon \beta^*} \times F, \quad (1.2)$$

where  $N_b$  is the number of particles per bunch ( $\mathcal{O}(10^{11})$ ),  $n_b$  is the number of bunches per beam,  $f_{\text{rev}}$  is frequency of revolution,  $\gamma$  is the Lorentz factor of the beam,  $\epsilon$  is transverse emittance of the beam,  $\beta^*$  is beta function of the beam at the collision point, and  $F$  is the geometric luminosity reduction factor due to the crossing angle at the interaction point. The instantaneous luminosity decreases exponentially as a function of time due to  $N_b$  and  $n_b$  being reduced by collisions. The LHC is designed to deliver an initial instantaneous luminosity of  $\mathcal{O}(10^{34}) \text{ cm}^{-2} \text{ s}^{-1}$ , achieved by having multiple inelastic proton-proton interactions per bunch crossing known as pileup.

As all known cross sections are time-independent, the total number of events is directly proportional to the integrated luminosity given by

$$L_{\text{int}} = \int_0^T dt L(t) = L(0)\tau_L (1 - e^{-T/\tau_L}), \quad (1.3)$$

where  $T$  is the time since starting collisions,  $L(0)$  is the initial instantaneous luminosity, and  $\tau_L \approx 15$  the characteristic beam loss timescale for the LHC. The total luminosity delivered by the LHC and recorded by CMS during the 2016 is shown in Figure 1-2.

## 1.2 Collider Phenomenology

The proton is a composite particle consisting of valence quarks, sea quarks, and gluons, collectively referred to as partons. When colliding protons at the LHC, we are actually interested in the inelastic scattering of a pair of partons from the incident protons. Each parton  $a, b$  carries a fraction of the momentum of the incoming proton  $x_{a,b}$  following the particle-dependent parton distribution functions (PDFs)  $f_{a,b}$ . The differential cross section for  $2 \rightarrow N$  parton scattering process is given by

$$d\sigma(ab \rightarrow \{c_i\}) = \frac{(2\pi)^4}{2s} \left( \prod_i \frac{d^3 p_i}{(2\pi)^3} \right) \cdot \delta^4 \left( k_a + k_b - \sum_i p_i \right) \cdot |\mathcal{M}(ab \rightarrow \{c_i\})|^2 \quad (1.4)$$

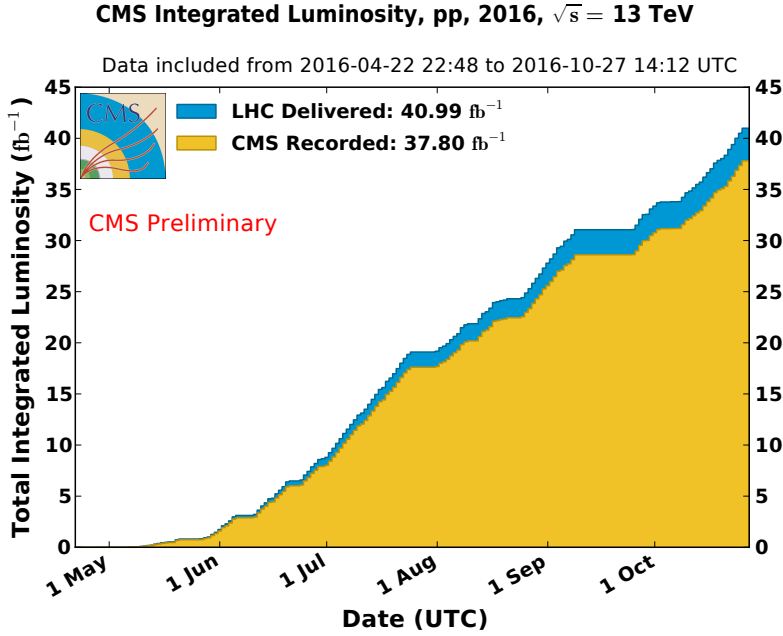


Figure 1-2: The total integrated luminosity of the LHC during proton-proton collisions during 2016.[] While a total luminosity of  $41 \text{ fb}^{-1}$  was collected, only a subset during which the detector operated optimally is used in this thesis. This corresponds to  $36 \text{ fb}^{-1}$  of data.

where  $k_{a,b} = x_{a,b}\sqrt{s}$  are the momenta of the incoming partons,  $\{p_i\}$  are the momenta of the outgoing partons  $\{c_i\}$ , and  $\mathcal{M}$  is the matrix element of the process.

This parton level scattering, called the hard scattering process, is perturbatively calculable through standard QFT methods. However, the hard scattering does not include any effects related to the PDFs of the incoming partons or the decay and hadronization of the outgoing partons into the final state particles (called the parton shower), both of which involve non-perturbative aspects of QCD. Fortunately, the collinear factorization theorem states that the probability of obtaining the final state  $X(\Theta)$  from a hadron collision can be calculated as the product of the probability that specific partons  $a, b$  are involved in the interaction, the probability for the hard scattering to produce outgoing partons  $\{c_i\}$ , and the formation of final state hadrons from these outgoing partons. The factorization process is not unique and requires the choice of an arbitrary energy scale  $\mu_F$ , which defines a lower bound for interactions to be considered part of the hard scattering.

Including the effects from PDFs and parton showering (PS), the general cross

section for  $pp \rightarrow X(\Theta)$  is

$$\begin{aligned} \frac{d\sigma}{d\Theta}(pp \rightarrow X(\Theta)) &= \sum_{a,b} \int dx_a f_a(x_a, \mu_F) \cdot dx_b f_b(x_b, \mu_F) \\ &\quad \times d\sigma(ab \rightarrow \{c_i\}) \times D(\{c_i\} \rightarrow X(\Theta)) \end{aligned} \quad (1.5)$$

where the sum is over the initial state partons and  $D$  is the fragmentation function that describes parton shower process resulting in the observed final state. The following sections discuss the simulation of the three main elements of Equation 1.5: the parton distribution functions  $f_a$ , the hard scattering cross section  $d\sigma$ , and the parton shower and hadronization processes that contribute to the fragmentation function  $D$ .

### 1.2.1 Parton Distribution Functions

Due to soft collinear emissions from the partons, the behavior of the parton distribution functions depends on the factorization scale. Denoting the gluon PDF as  $g(x, \mu_F)$  and the PDF for quark flavor  $i$  as  $q_i(x, \mu_F)$ , the analytic behavior of the PDFs is given by the DGLAP evolution equations

$$\mu_F \frac{d}{d\mu_F} \begin{pmatrix} q_i(x, \mu_F) \\ g(x, \mu_F) \end{pmatrix} = \frac{\alpha_s}{2\pi} \int_x^1 \frac{dy}{y} \begin{pmatrix} P_{qq}(x/y) & P_{qg}(x/y) \\ P_{gq}(x/y) & P_{gg}(x/y) \end{pmatrix} \begin{pmatrix} q_i(y, \mu_F) \\ g(y, \mu_F) \end{pmatrix} \quad (1.6)$$

where  $y$  is the fraction of momentum carried by initial parton and the  $P$  matrix elements are the splitting kernels defined by

$$\left| \begin{array}{l} P_{qq}(z) = \frac{4}{3} \left( \frac{1+z^2}{1-z} \right) \\ P_{qg}(z) = \frac{4}{3} \left( \frac{1+(1-z)^2}{z} \right) \\ P_{gq}(z) = \frac{1}{2} (z^2 + (1+z)^2) \\ P_{gg}(z) = 6 \left( \frac{1-z}{z} + \frac{z}{1-z} + z(1-z) \right). \end{array} \right. \quad (1.7)$$

The DGLAP equations cannot be solved analytically at a fixed scale. Instead, parameterized functional forms are fitted to data from many experiments. The results presented in this thesis use the NNPDF3.0 PDF set provided by the NNPDF collaboration.

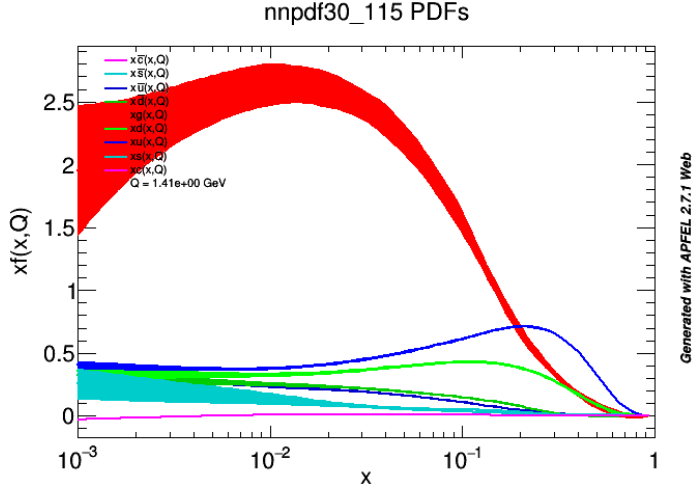


Figure 1-3: The various quark and gluon PDFs for the proton, as a function of momentum fraction  $x$ . The specific PDF set is the NNPDF3.0 118 NLO PDF set.

oration. Figure 1-3 shows the quark and gluon PDFs for the proton. As  $x \rightarrow 0$ , the gluon fraction dominates while as  $x \rightarrow 1$ , the up-quark fraction  $u(x, \mu_F)$  approaches  $\frac{2}{3}$ , the down-quark fraction  $d(x, \mu_F)$  approaches  $\frac{1}{3}$ , and the gluon and sea quark fractions approach zero.

### 1.2.2 Hard Scattering

The hard scattering process is simulated using Monte Carlo generators that sample events with probability proportional to the phase space and matrix element. For the results contained in this thesis, the primary hard interaction is simulated using the MADGRAPH5 aMC@NLO generator, which can simulate to leading order (LO) in EW vertices and up to next-to-leading order (NLO) in QCD vertices.

### 1.2.3 Parton Shower

The parton shower is a sequence of splittings where one outgoing parton  $c_i$  emits a second soft and/or collinear particle  $j$ . Each splitting has an associated splitting kernel  $P_{c_i \rightarrow c_i j}(z)$ , where  $z$  is the momentum fraction carried by the initial parton. The allowed QCD splittings are  $q \rightarrow qg$ ,  $g \rightarrow q\bar{q}$ , and  $g \rightarrow gg$  and the allowed QED

splittings are  $f \rightarrow f\gamma$  and  $\gamma \rightarrow f\bar{f}$ . The kernels associated with these splittings are

$$\left. \begin{array}{l} P_{q \rightarrow qg}(z) = \frac{4}{3} \left( \frac{1+z^2}{1-z} \right) \\ P_{g \rightarrow q\bar{q}}(z) = \frac{1}{2} (z^2 + (1-z)^2) \\ P_{g \rightarrow gg}(z) = 3 \left( \frac{(1-z)(1-z)^2}{z(1-z)} \right) \end{array} \right| \begin{array}{l} P_{f \rightarrow f\gamma}(z) = Q_f^2 \left( \frac{1+z^2}{1-z} \right) \\ P_{\gamma \rightarrow f\bar{f}}(z) = N_C Q_f^2 (z^2 + (1-z)^2) \end{array} \quad (1.8)$$

where  $Q_f$  is the charge of the fermion and  $N_C$  is the number of color states the fermion can occupy (3 for quarks and 1 for leptons). The cross section of a splitting is given by

$$\frac{d\sigma(ab \rightarrow \{c_i\}j)}{d\sigma(ab \rightarrow \{c_i\})} = P_{c_i \rightarrow c_ij}(z) \cdot \frac{\alpha_s}{2\pi} \cdot \frac{d\theta}{\theta} \cdot dz \quad (1.9)$$

where  $\theta$  is the opening angle between  $c_i$  and  $j$ . These cross sections diverge as  $\theta \rightarrow 0$  and  $z \rightarrow 1$ , meaning bare quarks producing many soft and collinear gluons. Then, these gluons further split to  $gg$  and  $q\bar{q}$  pairs, which in turn emit even more soft and collinear gluons and photons. This process continues until the energy of the outgoing partons reaches  $\Lambda_{\text{QCD}}$  at which point hadronization occurs.

#### 1.2.4 Hadronization

The QCD potential between two quarks can be approximated as  $V(\vec{r}) \approx \kappa r$ , where  $\kappa$  has been measured to be approximately 1 GeV/fm. The linear behavior of the potential is due to the attractive interactions between the gluons mediating the quark-quark interaction which confine the color field between the quarks into a tube 1 fm in diameter. As the quarks separate, the energy contained in this gluon tube increases linearly until it exceeds the mass of a  $q\bar{q}$  pair. At this point, a new  $q\bar{q}$  pair pops into existence through a quantum mechanical tunneling process, splitting the tube in two. Due to the difference in quark masses, only up, down, and strange quarks are produced, in a 10:10:3 ratio. This process continues until the energy of all the quarks have low enough energy to combine into stable hadrons.

The above procedure is a qualitative description of the Lund string model used. The Pythia event generator models hadronization using the Lund string model as

well as the parton shower effects described in the previous section. All results in this thesis use the Pythia 8.2 program to simulation the parton shower and hadronization processes.

# Chapter 2

## The CMS Detector

The Compact Muon Solenoid (CMS) detector is one of two hermetic, general purpose detectors at the Large Hadron Collider. The original motivation for the experiment was the discovery of the Higgs boson by observing its decays to photons, electrons, and muons. Towards this end, the detector was built to fulfill the following goals:

- Unambiguous charge identification of muons with momenta up to 1 TeV
- 1 GeV mass resolution on 100 GeV pairs of muons, electrons, and photons
- Efficient triggering and tagging of  $\tau$  lepton and  $b$  quark decays
- Good resolution on the hadronic energy and missing transverse energy
- Sufficient time resolution to deal with 40 MHz of collisions

The CMS detector consists of four main subdetectors: the inner trackers, the electromagnetic calorimeter (ECAL), the hadronic calorimeter (HCAL), and the muon chambers. The first three are within the field volume of the eponymous 3.8 T superconducting NbTi solenoid magnet while the muon chambers are embedded in the return yoke of the magnet. Additionally, there is an online triggering system to reduce readout from 40 MHz to  $\mathcal{O}(1)$  kHz for prompt reconstruction.

The overall layout of the CMS detector is shown in Figure 2-1. The CMS detector has a weight of 12500 tons, a length of 22 m, a diameter of 15 m, and a cylindrical

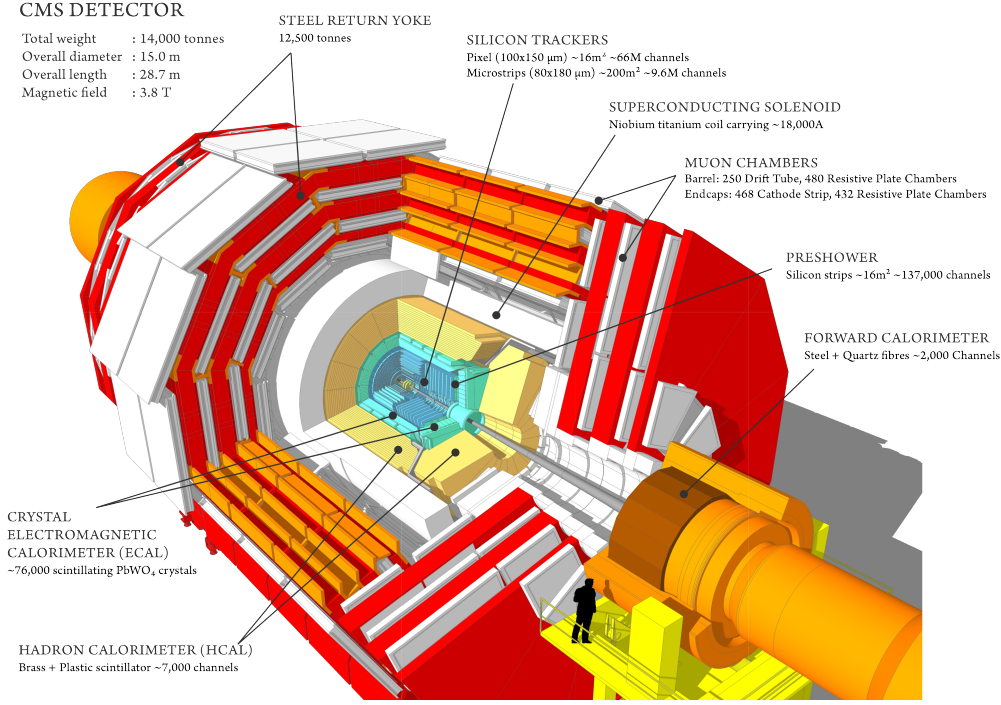


Figure 2-1: A cutaway view of the CMS detector. The labels identify the solenoid as well as the different subdetectors and their components. Reprinted from Reference [1].

geometry with concentric barrel shaped detectors in the central region and disc shaped detectors in the forward region. The following coordinate system is used when working with the CMS detector:

- distance  $z$  along the beam axis
  - $z = 0$  at the center of the detector
  - positive corresponds to counter-clockwise as seen from the sky
- distance  $r$  from the beam axis
- polar angle  $\theta$  measured with respects to the positive  $z$ -axis
- azimuthal angle  $\phi$  in the plane orthogonal to the beam axis

In addition to these four main coordinates, we define the right-handed cartesian  $x$  and  $y$  coordinates perpendicular to the beam axis, with the positive  $x$ -axis pointing

from the center of the detector to the center of the LHC ring and the positive  $y$ -axis pointing upwards.

The four-momentum of a particle is  $p = (p_x, p_y, p_z, E)$  in the cartesian basis and a particle of mass  $m$  produced at rest in the center of the detector has  $p = (0, 0, 0, m)$ . While the momenta along the beam axis of the two incoming protons are equal, the momenta of the incoming partons involved in the hard scattering often are not as discussed in Section 1.2. Thus, we define two kinematic quantities that are Lorentz-invariant with respect to a boost along the beam axis: the transverse momentum  $\vec{p}_T = p_x \hat{x} + p_y \hat{y}$  with magnitude  $p_T = \sqrt{p_x^2 + p_y^2}$  and the pseudorapidity  $\eta = -\ln \tan \theta/2$ .

In terms of  $p_T$ ,  $\eta$ , and  $\phi$ , we have the following expressions for our cartesian variables:  $p_x = p_T \cos \phi$ ,  $p_y = p_T \sin \phi$ ,  $p_z = p_T \sinh \eta$ , and  $E = p_T \cosh \eta$ , with the last equality assuming the mass of the particle is negligible compared to its momentum. In terms of our Lorentz-invariant coordinates, the four-momentum of a given particle is  $p = (p_T, \eta, \phi, E)$ . Additionally, the spatial separation of two particles is given by  $\Delta R = \sqrt{(\Delta\phi)^2 + (\Delta\eta)^2}$  and the fiducial acceptance of the CMS detector is from  $0 \leq \phi < 2\pi$  and  $-5 \leq \eta \leq 5$ .

## 2.1 Inner Trackers

Closest to the interaction point, the inner trackers identify charged particles and measures their momenta. Additionally, high resolution tracks are used to identify primary and secondary vertices. The magnetic field in the tracker volume is uniform with strength 3.8 T and field lines parallel to the beam direction. The tracker volume extends to 1.2 m in  $r$  and 2.9 m in  $z$ , providing coverage for  $|\eta| < 2.5$ , and is instrumented with silicon pixels and strips. Each silicon sensor is a  $p$ - $n$  semiconductor junction with a bias voltage applied. When a charged particle passes through the depletion region of the junction, electron-hole pairs are produced and collected by the readout electronics. A schematic of the inner tracker system is shown in Figure 2-2.

The 66 million individual pixel sensors, each measuring  $285 \mu\text{m} \times 100 \mu\text{m} \times 150 \mu\text{m}$  in  $r \times r\phi \times z$ , are arranged into seven layers: three cylindrical barrels at  $r =$

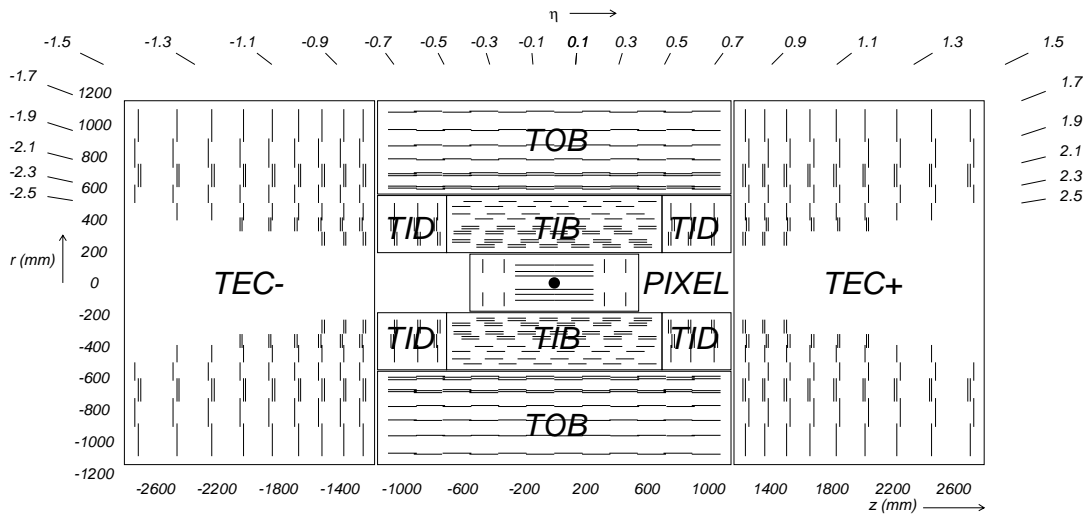


Figure 2-2: A schematic view of the CMS inner tracker system. Silicon pixel and strip detectors are shown. The volumes labeled TIB, TID, TOB, and TEC are all strip trackers. The double lines indicate back-to-back modules that deliver stereo hits. Reprinted from Reference [1].

4.4, 7.3, 10.2 cm and two bi-layer endcap annuli at  $z = \pm 34.5, \pm 46.5$  cm. Due to the geometry of the pixel detector, tracks typically cross the sensor at a  $20^\circ$  angle, leading to the charge deposit from a single track to be shared among multiple pixels in the same layer. The exact position of a particle in each layer is determined by interpolating the signals from multiple adjacent pixels with an analog pulse height greater than a tuneable read-out threshold. Thus, each pixel hit is localized to an area of  $\sim 15\text{ }\mu\text{m} \times 20\text{ }\mu\text{m}$  in  $r\phi \times z$ , providing a much higher spacial resolution than the raw pixel spacing.

The pixels are surrounded 9.3 million silicon strips measuring  $10\text{ cm} \times 80\text{ }\mu\text{m}$  arranged in ten cylindrical layers in the barrel and twelve disks in each endcap. The Tracker Inner Barrel (TIB) consists of the first four layers and extends from 20 cm to 55 cm in the radial direction while out six layers constitute the Tracker Outer Barrel (TOB) with an outer radius of 116 cm and extent in  $|z|$  of 118 cm. The remaining area in the barrel is covered by the Tracker Inner Disk (TID), consisting of the three disks located from 80 to 90 cm in  $|z|$ . The Tracker EndCaps (TEC) have nine disks each and cover the region  $124\text{ cm} < |z| < 282\text{ cm}$ .

The majority of the strips are oriented perpendicular to the  $\phi$  direction: parallel to the beam pipe in the barrel region and radially aligned in the endcap region. The strip pitch varies from 80 to 184  $\mu\text{m}$  with the smallest pitch in the innermost layer. This detector geometry provides good resolution in the  $r$ - $\phi$  plane for barrel and the  $z$ - $\phi$  plane for the endcap but little information on the orthogonal directions. To compensate for this, one third of the strips are double-layered with a stereo angle of 100 mrad between the layers. Matching hits between adjacent layers enables a measurement of the  $z$  and  $r$  coordinates in the barrel and endcap, respectively. The final spacial resolution is 10-50  $\mu\text{m}$  in the direction perpendicular to the strips and 100-530  $\mu\text{m}$  in the parallel direction on the stereo modules.

## 2.2 Electromagnetic Calorimeter

The electromagnetic calorimeter (ECAL) is a homogeneous, hermetic calorimeter composed of 76,000 lead tungstate ( $\text{PbWO}_4$ ) crystals. High density (8.3 g/cm<sup>3</sup>) lead tungstate was chosen due to its radiation hardness, fast scintillation decay time constant of 25 ns, small Moliere radius  $r_M = 21.9$  mm, and short radiation length  $X_0 = 8.9$  mm. All of these factors combine to enable the construction of a compact calorimeter with high granularity and excellent energy resolution.

Figure 2-3 shows the layout of the ECAL. The central barrel region (EB) has 61200 crystals arranged in a  $170 \times 360$   $\eta$ - $\phi$  grid (0.0174  $\times$  0.0174 granularity) with a coverage up to  $|\eta| = 1.44$  while the two endcap annuli (EE) each have 7324 crystals organized in a  $x$ - $y$  grid with coverage in the range  $1.479 < |\eta| < 3.0$ . Each crystal in the EB has a truncated pyramidal shape with a length of 230 mm, a 22 mm  $\times$  22 mm front-face cross-section, and a 26 mm  $\times$  26 mm rear-face cross-section while a crystal in the EE has a cuboid-like shape with a length of 220 mm, a 28.6 mm  $\times$  28.6 mm front-face cross-section, and a 30 mm  $\times$  30 mm rear-face cross-section. The cross-sectional area of approximately one Moliere radius and length of approximately 25 radiation lengths allows just a few crystals to contain the entire transverse and longitudinal development of the shower. To reduce the likelihood of the primary photon or electron

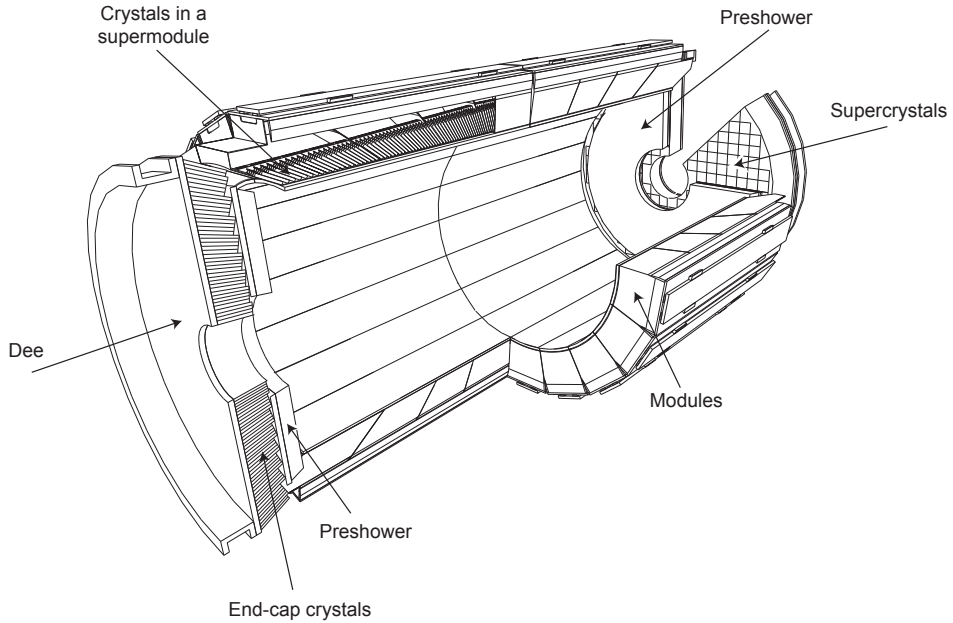


Figure 2-3: The layout of the CMS electromagnetic calorimeter. The barrel and endcap calorimeters are shown. The pre-shower detector sits in front of the endcaps. Reprinted from Reference [1].

emerging from the hard scattering depositing most of its energy in passive material, the crystals do not point directly to the interaction region.

The interactions between the 3.8 T magnetic field and the geometries of the ECAL lead to the selection of different photosensors in the barrel and endcaps. In the endcaps, the magnetic field is parallel to the path of the photoelectrons and has a negligible effect on the gain, while in the barrel, the magnetic field is perpendicular and reduces the gain by a factor proportional to the distance traveled by the photoelectrons. Thus, in the barrel, solid-state reverse-structure avalanche photodiodes (APDs) with a depletion layer of  $6.0 \pm 0.5 \mu\text{m}$  are used, while photomultiplier tubes with a single gain stage and a very fine copper mesh anode called vacuum phototriodes (VPTs) are used in the endcaps. Two APDs with an active area of  $25 \text{ mm}^2$  are glued to the rear of each crystal in the barrel while only one VPT with an active area of  $280 \text{ mm}^2$  is needed per crystal in the endcap. The APDs and VPTs amplify the initial signal of approximately 4.5 photoelectrons per MeV of energy deposit per

crystal by a factor of 50 and 10, respectively.

The small signals from the photodetectors are shaped and amplified in the Multi-Gain Preamplifier (MGPA) and a 12-bit analog-to-digital converter (ADC) samples the pulse every 25 ns. Each output voltage pulse has a length of approximately 300 ns, with the maximum at approximately 75 ns and a slow decay afterwards. The MGPA has multiple gain modes of 12, 6, and 1, and the gain chosen for the output decreases once the signal has saturated the previous gain setting. After the pulse falls below the saturation threshold, the lower gain setting is maintained for the next five samples. This mechanism provides a dynamic signal range from a few MeV to a maximum of 1.5 TeV in the barrel and 3.1 TeV in the endcaps.

The energy resolution of the ECAL was measured using an electron beam to be

$$\frac{\sigma_E}{E} = \frac{2.8\%}{\sqrt{E/\text{GeV}}} \oplus \frac{12\%}{E/\text{GeV}} \oplus 0.3\%, \quad (2.1)$$

where  $E$  is the energy of the incident particle and the three terms on the RHS are the stochastic, noise, and constant terms, respectively. The stochastic term is dominated by event-to-event fluctuations in the lateral shower containment and a photo-statistics contribution of 2.1%. Electronic and digitization noise drive the noise term while the constant term comes from a non-uniform longitudinal light collection and intercalibration errors.

### 2.2.1 Preshower Detector

At high momenta and high  $|\eta|$ , the two photons from a  $\pi^0$  decay can merge into a single ECAL crystal due to the large boost in the  $z$ -direction of the initial state. By forcing the initiation of an electromagnetic shower in a region with high spacial resolution in front of the ECAL endcaps, the preshower detector can differentiate between one- and two-photon deposits in the region  $1.6 < |\eta| < 2.5$ . The preshower detector consists of two alternating layers of passive lead absorbers and active silicon strip sensors. The first (second) lead layer is two (one) radiation lengths thick and the subsequent sensor plane has vertical (horizontal) strips of 6 cm length and 1.9 mm

pitch. The silicon strips resolve the shower with a resolution of  $\mathcal{O}(1\text{--}10)$  mm, enabling the disambiguation of two nearly collinear photons and the identification of  $\pi^0$  decays.

## 2.3 Hadronic Calorimeter

The hadronic calorimeter (HCAL) is a set of four heterogenous calorimeters that provide hermetic coverage when combined: the barrel calorimeter (HB) covering  $|\eta| < 1.3$ , the endcap calorimeter (HE) covering  $1.3 < |\eta| < 3$ , the outer calorimeter (HO) covering  $|\eta| < 1.3$ , and the forward calorimeter (HF) covering  $3 < |\eta| < 5$ . The region covering  $|\eta| < 3$  shall be referred to as the central HCAL. The granularity of the HCAL in  $\eta\text{-}\phi$  is  $0.087 \times 0.087$  for  $|\eta| < 1.6$ ,  $0.17 \times 0.17$  for  $1.6 < |\eta| < 3.0$ , and  $0.175 \times 0.175$  for  $3 < |\eta| < 5$ . The layout of the HCAL is shown in Figure 2-4.

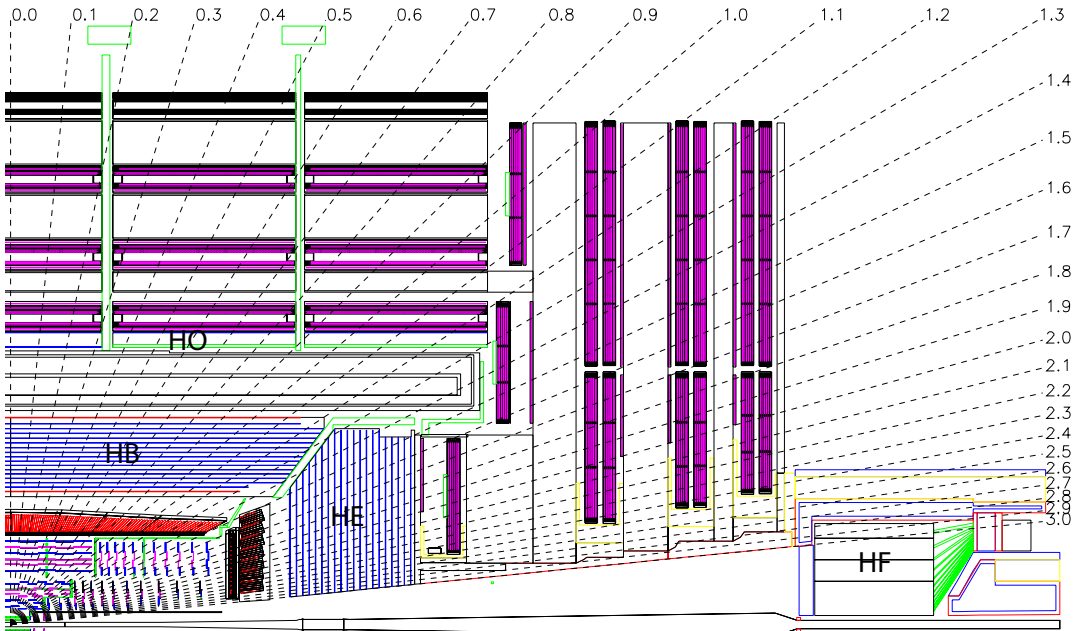


Figure 2-4: The layout of the CMS hadronic calorimeter. The barrel, endcap, outer, and forward calorimeters are shown and labeled. The muon chambers are shown but not labeled. The dashed lines denote different values of pseudorapidity. Reprinted from Reference [1].

The HB and HE are sampling calorimeters with 16 and 17 thin plastic scintillator

layers, respectively, interleaved with thick absorber layers made of a non-magnetic brass alloy with an interaction length  $\lambda_I = 1.5$  cm. The layers range in thickness from 40 to 75 mm providing a total absorber depth ranging from a minimum of 5.82  $\lambda_I$  at  $|\eta| = 0$  to a maximum of 10.6  $\lambda_I$  at  $|\eta| = 1.3$  in the barrel and approximately nine interaction lengths throughout the endcaps, with the ECAL contributing another interaction length worth of material. The dimensions of the HB and HE are determined by the requirement that they reside between the ECAL and the solenoid. To circumvent this constraint, an additional layer of scintillator located in the return yoke of the magnet, the HO, utilizes the solenoid material as an additional interaction length of absorber. Hybrid photodiodes (HPDs) are used to read out the scintillator light in the HB and HE while silicon photomultipliers (SiPMs) are used in the HO.

Located 11 meters from the interaction point, the HF is a sampling calorimeter covering the region of phase-space with high pseudorapidity. Since the particle flux here is much higher than in the central region, the HF uses radiation-hard steel absorber instrumented with two sets of scintillating quartz fibers. Charged particles produced by showers in the steel traverse the quartz fibers and emit Cherenkov radiation that is recorded by photomultiplier tubes. To distinguish hadrons from photons and electrons, the second set of fibers starts at a depth of 22 cm.

Since hadrons interact with the ECAL as well as the HCAL, the energy resolution of the detectors must be considered in tandem in the central region. Using a charged particle test beam, the combined ECAL+HCAL energy resolution was measured to be

$$\frac{\sigma_E}{E} = \frac{0.847}{\sqrt{E/\text{GeV}}} \oplus 0.074 \quad (2.2)$$

and the standalone HF energy energy resolution is

$$\frac{\sigma_E}{E} = \frac{1.98}{\sqrt{E/\text{GeV}}} \oplus 0.09. \quad (2.3)$$

## 2.4 Muon Chambers

The outer most components of CMS are the muon triggering, identification, and detection chambers. These muon detectors are interleaved with the steel return yoke of the magnet resulting in a characteristic *S*-shape for the muon trajectories due to the reversal of magnetic field direction across the solenoid. Signal purity in the muon detectors is high as hadrons, electrons, and photons are stopped by the calorimeters while muons are minimum ionizing particles (MIPs) that lose little energy while traversing the detector. Taking advantage of the large detector volumes required by the outer solenoid radius of 3.5 m, three types of gas ionization chambers are used: drift tubes (DTs) in the barrel covering  $|\eta| < 1.2$ , cathode strip chambers (CSCs) in the endcaps covering  $0.9 < |\eta| < 2.4$ , and resistive plate chambers (RPCs) in both covering  $|\eta| < 2.1$ . The layout of the muon detectors is shown in Figure 2-5.

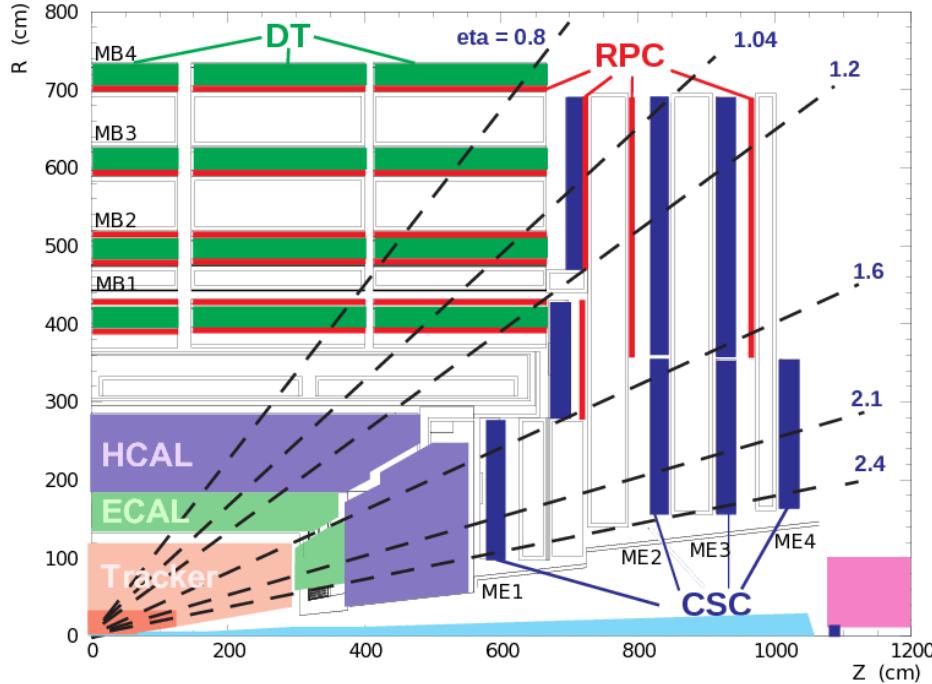


Figure 2-5: The layout of the CMS muon chambers. The four DT stations are labeled MB1-MB4, the four CSC stations are labeled ME1-ME4, and the RPC stations are shown in red. The dashed lines denote different values of pseudorapidity. Reprinted from Reference [1].

The DT chambers consist of rectangular drift cells with transverse dimensions of  $42\text{ mm} \times 13\text{ mm}$  filled with a 85:15 Ar/CO<sub>2</sub> mix and a gold/steel anode wire held at a voltage of 3.6 kV. The maximum drift time per cell of 400 ns provides a spatial resolution of approximately 250  $\mu\text{m}$ . A single chamber is made out of superlayers which are in turn made out of four individual cells for a combined resolution of 100  $\mu\text{m}$ . The chambers are arranged into four 2.4 m thick dodecagonal rings called the muon barrel stations. All four stations have two superlayers per chamber that measure position in the  $r\text{-}\phi$  plane while the chambers in the inner three stations have an additional superlayer that measures position in the  $r\text{-}z$  plane. Together, the four muon stations and iron yokes form a wheel with one between the solenoid and the first iron layer, two in between the yokes, and one outside. The outer barrel is composed of five wheels in total.

Due to their faster response time and better spatial resolution, CSCs are used to handle the higher muon and background fluxes in the endcap region. Each CSC is filled with a 50:40:10 CO<sub>2</sub>/Ar/CF<sub>4</sub> mix and instrumented with 80 cathode strips held at voltages of 2.9–3.6 kV relative to the gold-plated tungsten anode wires. The strips run radially outward to measure position in the  $r\text{-}\phi$  plane while the wires run perpendicular measure the  $\eta$  and beam-crossing time of the muons. The four muon stations in each endcap are made of CSCs arranged into annuli oriented perpendicular to the beam axis and interspersed between the flux return plates. The three inner stations have multiple annuli with smaller ones fitting inside the larger ones while the fourth station only has one close to the beamline.

An RPC is a parallel-plate double-gap chamber with a time resolution of one nanosecond and a poor spatial resolution. The RPCs are interspersed throughout the DT and CSCs to provide an independent muon trigger system that can identify the correct bunch crossing time.

## 2.5 Online Trigger System

To achieve an instantaneous luminosity of  $\mathcal{O}(10^{34}) \text{ cm}^{-2} \text{ s}^{-1}$ , the LHC has bunch crossings every 25 ns for a total data rate of 40 MHz, much higher than the 100 kHz readout rate for the detector and the  $\mathcal{O}(1)$  kHz data reconstruction and tape writing rates. Fortunately, uninteresting elastic scattering and QCD inelastic scattering events dominate the approximately  $100 \mu\text{b}$  total proton-proton cross-section at the LHC. Meanwhile, most new physics processes have a predicted on the order of picobarns or femtobarns and even the highest rate SM EWK cross-sections are  $\mathcal{O}(10)$  nb, so not every event needs to be readout, reconstructed, and written to tape.

A two-stage trigger system selects the events to keep for permanent storage and analysis. The Level 1 hardware-based trigger (L1) selects interesting events based on incomplete detector information to reduce readout and computation times. Events selected by the L1 trigger are fully readout and passed to the high level software-based trigger (HLT). The HLT reconstructs the full event on a CPU farm using a version of the offline reconstruction software optimized to process a single event within 200 ms at the cost of precision. Events selected by the HLT are sent to the offline computing resources for full reconstruction followed by storage on disk and tape.

The L1 trigger uses field programmable gate arrays (FPGAs) and application specific integrated circuits (ASICs) to make decisions within  $4 \mu\text{s}$  of each collision. Each subdetector module has a hardware trigger that reconstructs objects called trigger primitives (TPs). In the two calorimeters, clustered energy deposits from each tower are sent to a regional calorimeter trigger (RCT) which correlates the information from adjacent towers and between the ECAL and HCAL into electron, photon, and jet candidates. The outputs from the RCT are passed to the global calorimeter trigger (GCT) which computes global event variables such as the total transverse energy, the hadronic transverse energy, and the momentum imbalance. Muon track candidates are produced from a simple segment-finding and tracking algorithm in each of the three types of muon chambers. The global muon trigger (GMT) receives the candidates and combines them with information from the GCT

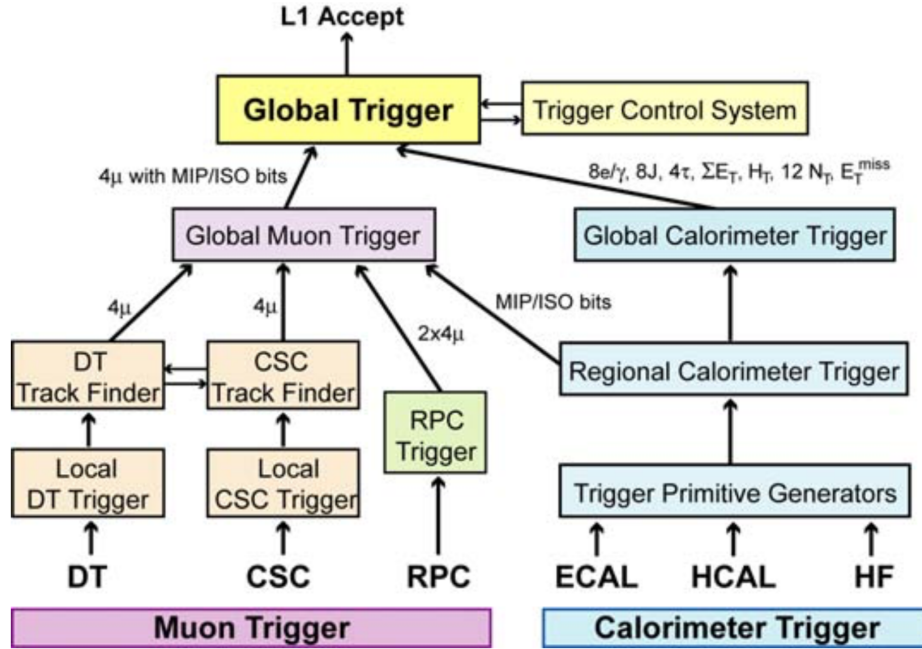


Figure 2-6: The Level-1 trigger architecture with components labeled and information flow indicated. Reprinted from Reference [1].

to produce the final set of muon candidates. The global trigger (GT) decides if an event should be sent to the HLT based on the information it receives from the GCT, the GMT, and the Timing, Trigger, and Control (TTC) system that monitors the readiness of the sub-detectors and the data acquisition (DAQ) system. The inner tracker is not included because the detector readout and reconstruction process take longer than the time allotted. Figure 2-6 shows a schematic description of the full L1 trigger process.

## 2.6 Detector Simulation

The Geant4 program is used to simulate the detector response to the particles produced in collisions. Starting with the output of the particle-level MC described in Section 1.2, final state particles are propagated through the solenoid's magnetic field into the passive and active elements of the detector where energy deposition, decay, and showering are simulated. Additional inelastic proton-proton collision are overlaid

into an event to simulate the effects of pileup. As the particles interact with the detector, the response of the readout electronics is simulated, including the effects of noise. In order to minimize differences between simulated events and those from collisions, the reconstruction software and output format are the same for both up to the retention of additional truth information from the generators.